ACS APPLIED MATERIALS & INTERFACES
Research Article
www.acsami.org

Interface Architecture for Superthick Carbon-Based Films toward Low Internal Stress and Ultrahigh Load-Bearing Capacity

Junjun Wang,[†,‡] Jibin Pu,[†] Guangan Zhang,[†] and Liping Wang*[,†]

[†]State Key Laboratory of Solid Lubrication, Lanzhou Institute of Chemical Physics, Chinese Academy of Sciences, Lanzhou 730000, People's Republic of China

[‡]University of Chinese Academy of Sciences, Beijing 100039, People's Republic of China

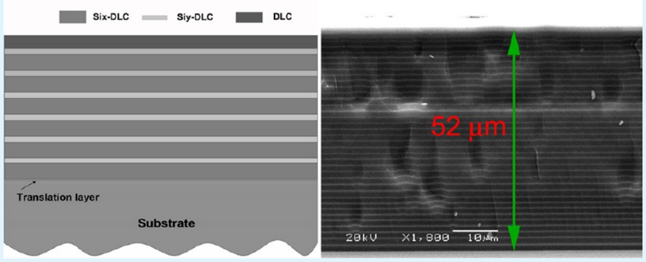

ABSTRACT: Superthick diamond-like carbon (DLC) films [(Si_x-DLC/Si_y-DLC)$_n$/DLC] were deposited on 304 stainless steel substrates by using a plane hollow cathode plasma-enhanced chemical vapor deposition method. The structure was investigated by scanning electron microscopy and transmission electron microscopy. Chemical bonding was examined by Raman, Auger electron, and X-ray photoelectron spectroscopy techniques. Mechanical and tribological properties were evaluated using nanoindentation, scratch, interferometry, and reciprocating-sliding friction testing. The results showed that implantation of a silicon ion into the substrate and the architecture of the tensile stress/compressive stress structure decreased the residual stress to almost 0, resulting in deposition of (Si_x-DLC/Si_y-DLC)$_n$/DLC films with a thickness of more than 50 μm. The hardness of the film ranged from 9 to 23 GPa, and the adhesion strength ranged from 4.6 to 57 N depending on the thickness of the film. Friction coefficients were determined in three tested environments, namely, air, water, and oil. Friction coefficients were typically below 0.24 and as low as 0.02 in a water environment. The as-prepared superthick films also showed an ultrahigh load-bearing capacity, and no failure was detected in the reciprocating wear test with contact pressure higher than 3.2 GPa. Reasons for the ultrahigh load-bearing capacity are proposed in combination with the finite-element method.

KEYWORDS: *superthick DLC film, load-bearing capacity, finite-element method*

1. INTRODUCTION

Diamond-like carbon (DLC) films exhibit excellent properties such as high hardness, high wear resistance, low friction coefficient, and biological inertness. DLC films have attracted significant attention for use in various industrial applications because of these exceptional properties.[1−6] Particularly, DLC films on steel substrates have drawn considerable interest because of their existing and potential commercial importance such as drills, bearings, gears, molds, punches, medical implants, seals, and instruments.[7−9] The thickness of the DLC films is an important parameter to consider in these applications.[10−12] Continuous wear of the coated surface tends to form a film as thick as possible to prevent wear penetration.[13] In terms of load-bearing capability, the coating thickness must be maintained to avoid delamination. A thicker coating provides greater stress shielding for the softer substrate and protects the substrate from plastic deformation. The thicker the coating, the higher its load-bearing capability.[14] However, when DLC films are deposited on steel substrates, high intrinsic stress of several gigapascals higher[15,16] and a mismatch in the chemical bonding between the films and substrates often cause for poor adhesion, limiting the film thickness to a range between 1 and 3 μm.[17−20] Thus, the design and development of thick DLC films on steel substrates, which significantly increase the lifetime and load-bearing capability of steel mechanical components, are most important in fundamental research and industrial applications.

Design requirements for a thick DLC film include improvement of the interfacial adhesion strength between the DLC film and substrate as well as reduction of residual stress in the DLC film. A possible approach to improving the interfacial adhesion strength involves the introduction of a graded interface between the film and substrate. The graded interface can reduce the mismatch in the chemical bonding between the films and substrates. To overcome thickness limitation, Silva et al.[21] subjected the steel substrate to a series of pretreatments prior to deposition, including carbonitriding and carburizing of the steel substrate. They indicated that a graded interface was obtained using this series of pretreatments. This graded interface reduced the interfacial free energy and decreased the mismatch between the film and substrates, thereby increasing the work of delamination and improving the film adhesion. However, the thickness of the film remained at only 1.5 μm. Tarrant et al.[22] showed that carbon films can be enhanced by introducing a carbon composition gradient layer on various metallic substrates by ion implantation. Finally, carbon films with thicknesses as large as 4.6 μm can be deposited on silicon (Si) with good adhesion. Schwarz et al.[23] prepared a Si/silicon carbide (SiC)/DLC-graded film on a Titan substrate, with a

Received: March 4, 2013
Accepted: May 13, 2013
Published: May 13, 2013

dx.doi.org/10.1021/am400778p | ACS Appl. Mater. Interfaces 2013, 5, 5015−5024

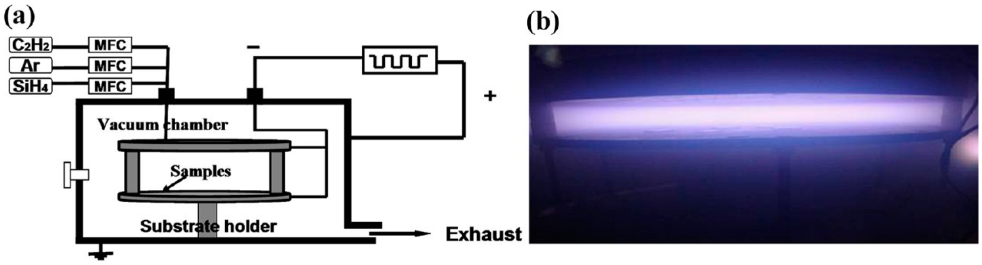

Figure 1. (a) Schematic of the deposition system and (b) aphotograph of the process in deposition progress.

thickness of up to 20 μm. This film also exhibits higher hardness, low elastic modulus, and no abrasion wear. However, these films have up to 11 μm thickness peel off during bending tests.

Doping with another element such as aluminum[24] or silver[25] or nonmetals such as Si or nitrogen[26−28] can alternatively reduce residual stress in the DLC film. Si is the most frequently used doping element. The effects of Si addition into the DLC films are attributed to Si−C formation. The difference in the bond lengths between Si−C (1.89 Å) and C−C (1.54 Å) can relieve stress in a longer-range order.[29] A further design possibility for reducing residual stress is growing coatings with a multilayer architecture, which has been intensively developed for metal and ceramic systems.[30] In addition, a multilayer structure is known to improve film toughness because cross-sectional cracks can be terminated by their deflection at interfaces and braking in a ductile layer with energy dissipation by plastic deformation.[31] The combined superthick characteristics of the film greatly enhance its load-bearing capacity. With the amorphous features of the DLC film considered, the development of techniques for reducing residual stress and deposit of a superthick DLC film by using the concept discussed in the literature remain a challenge.

The present study proposed the fabrication of superthick DLC films on steel substrates for wider application in potential engineering. The possibilities of fabricating superthick DLC films on steel substrates by using a plane hollow cathode plasma-enhanced chemical vapor deposition (PHC-PECVD) method were investigated. A detailed analysis of the characterization and testing of the deposited DLC films, as well as an overview of the range of properties that can be achieved, was performed.

2. MATERIALS AND METHODS

2.1. PHC-PECVD System. (Si_x-DLC/Si_y-DLC)$_n$/DLC films with different thicknesses were deposited on 304 stainless steel and P (1 0 0) Si substrates by a PHC-PECVD method. Figure 1 presents a schematic of the deposition system (Figure 1a) and the process of deposition (Figure 1b). The deposition system consists of a stainless steel vacuum chamber fitted with two parallel-plate electrodes. Under suitable vacuum conditions, applying a train of negative voltage pulses between −1 and −15 kV to two parallel-plate electrodes generates a pulsed glow discharge plasma. The positive ion in plasma is accelerated toward the substrate surfaces. Notably, energetic positive-ion bombardment can be controlled by the magnitude of the applied voltage and pressure. Secondary electrons are simultaneously generated by these energetic positive-ion impacts. These electrons do not escape from the two plates the first time. Instead, they oscillate across the opposing cathode plates, resulting in multiple ionizing collisions. The electrons move into the chamber wall to complete the circuit loop after a period of time. Consequently, high-density plasma is obtained. When the ion energy is high, ions are implanted into the surface; otherwise, the particles gather on the surface to form a thin film.

2.2. Sample Preparation. (Si_x-DLC/Si_y-DLC)$_n$/DLC film deposition consists of the following steps: (1) The substrates are cleaned ultrasonically in ethanol and acetone baths in succession and then dried with nitrogen. The substrates are placed in a vacuum chamber, and then the chamber is pumped down to a low pressure (1.3×10^{-4} Pa). Substrates are presputtered at a pressure of 1.5 Pa for 15 min with a constant flow of argon (Ar) gas fed into the chamber. The substrate bias voltage is adjusted to a pulse amplitude of −800 V, a duty cycle of 30%, and a repetition frequency of 1500 Hz. (2) Silane (SiH_4) and Ar gases are introduced into the chamber to produce a transition layer, where the substrate bias voltage is changed to a pulse amplitude of −1800 V, a duty cycle of 30%, and a repetition frequency of 1500 Hz. These intermediate layers effectively reduce stress, thus increasing their adhesion strength. (3) A multilayered film consisting of (Si_x-DLC/Si_y-DLC)$_n$ is fabricated by repeated synthesis of Si_x-DLC (low-Si-doped DLC layer) and Si_y-DLC (high-Si-doped DLC layer, $x < y$); n is the number of (Si_x-DLC/Si_y-DLC) layers. (4) A pure DLC film is deposited on (Si_x-DLC/Si_y-DLC)$_n$ as the surface layer. The thickness of the (Si_x-DLC/Si_y-DLC)$_n$/DLC coating is dependent on n. The gases include SiH_4 (50 sccm for Si_x-DLC and 100 sccm for Si_y-DLC), Ar (100 sccm), and acetylene (150 sccm for Si_x-DLC and 50 sccm for Si_y-DLC). The substrate bias voltage is maintained at −600 V, a duty cycle of 30%, and a repetition frequency at 1500 Hz. No external heating of the substrate was employed, and the maximum temperature during deposition was about 180 °C.

2.3. Film Characterization. The morphology and thickness of coated specimens were measured with cross-sectional scanning electron microscopy (SEM; JSM-5310, JEOL) observations. Surface profilometry (Alpha-step IQ, USA) was also used to confirm the thicknesses of the as-prepared coatings. The microstructure of the interface between the DLC film and substrate was examined in detail by high-resolution transmission electron microscopy (HRTEM; JEM-4000EX, JEOL) and scanning transmission electron microscopy (STEM, JEM-3000F, JEOL) observations and fast Fourier transform (FFT) diffraction patterns in combination. The sample for STEM observations was prepared by using a focused-ion beam (FB 2100, Hitachi). The composition of the film determined by X-ray photoelectron spectroscopy (XPS) and Auger electron spectroscopy (AES) is also used to characterize the film−substrate interface. The XPS spectra were acquired by employing a PHI-5700 instrument with unmonochromatized Mg Ka radiation ($h\nu$ = 1253.6 eV). The experimental resolution was 0.125 eV. A calibrated Hysitron Triboindenter with a Berkovich indenter was employed to determine the film hardness (H) and Young's modulus (E). A maximum load of 10 mN was used in order to ensure that the indention depth was within 10% of the film thickness. Six repeated measurements were made for each specimen. The residual stress was measured by stress-induced bending on an interferometric surface profiler. The curvature radii of the substrate before and after film deposition were measured by the observation of Newton's rings using an optical interferometer system, and then the residual stress was calculated by the Stoney equation. The adhesion of the sample was tested by a scratch tester (CSEM Revetest) equipped with a diamond tip of radius 200 μm. The normal load was increased from 0 to 100 N at a loading rate of 100 N/min and a scratching speed of 10 mm/min. During the scratch test, the acoustic emission and friction force were continuously monitored. The tribological properties of the as-deposited superthick (Si_x-DLC/Si_y-DLC)$_n$/DLC films were determined by a reciprocating wear test under different lubricated conditions, namely, air, water, and oil. The counterpart was a hardened (HRC 60-62) GCr 15 steel ball with a diameter of 6 mm. The sliding speed was 50 mm/s, and the normal load was 10 N. All of the tests were conducted at room temperature of about 24 ± 2 °C and a relative humidity of 20−30%. In order to detect the load-bearing capability, a test procedure was conducted at room temperature of about 24 ± 2 °C and a relative humidity of 20−30% under an air environment. A sliding speed of 50 mm/s was adopted in which a constant load was applied for 60 min. If there was no sudden change in the friction force during testing, it indicated that there was no damage to the specimen. Thus, another test with an increased load on a new track was completed. This process was undertaken until the friction force data suddenly increased, indicating that the surface coating failed. The maximum load that the specimen could withstand without failure indicated the load-bearing capacity. A noncontact 3D surface profiler (model MicroMAXTM, made by ADE Phase Shift, Tucson, AZ) was used to capture 3D images on a wear track for measurement of the wear volume. Five profilometry traces were taken on each wear surface to obtain wear depths and cross-sectional areas. The wear rate of the films is defined as the wear surface volume divided by the load and the total distance traveled by the counterface ball. Wear surfaces were examined by a JSM-5600 scanning electron microscope.

2.4. Finite-Element Method (FEM). The system of ball indentation onto a coated specimen considered in this study is illustrated in Figure 2. Despite the performance in the static mode, these simulations improve our understanding of the high load-bearing capability. The counterbody was assumed as perfectly rigid, and the transition layer was not considered. The film was assumed to be an isotropic, linear elastic material. Young's moduli of the coating were measured by a Hysitron TriboIndenter. The substrate was modeled as an isotropic, rate-independent solid with a bilinear elastic−plastic constitutive relationship, assuming kinematic strain hardening and the von Mises yield criterion. Table 1 lists the selection of parameters. n values of the (Si_x-DLC/Si_y-DLC)$_n$/DLC film were set at 1, 6, 24, and 44 with corresponding thicknesses of 2.6, 9.6, 34.8, and 62.8 μm, respectively.

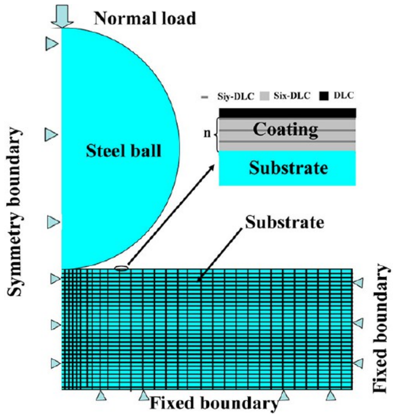

Figure 2. Finite-element model of the (Si_x-DLC/Si_y-DLC)$_n$/DLC-coated substrate, with detail of the mesh at the edge of the contact region.

Table 1. Material Properties Used in FEM Simulations

	film thickness (μm)	Young's modulus (GPa)	Poisson's ratio
substrate	3000	193	0.3
Si_x-DLC	1.2	82	0.25
Si_y-DLC	0.2	150	0.25
DLC	1.2	88	0.25

For comparison, the same quantity of pressure was applied. An axisymmetric system was assumed; thus, only half of the geometry was modeled. The mesh was arranged in an eight-node brick element and was specifically formulated to model large deformation with plastic behavior. To resolve properly high-stress gradients under the indenter and an accurate detection of the contact nodes, a very fine mesh was used locally near the contact area, with an element size of $t/10$ (t is the thickness of the film). Surface-to-surface contact elements CONTA175 were used for deformable materials, whereas a TARGE169 element provided the counterbody that was assumed to be perfectly rigid. The contact friction was assumed to be zero, which was reasonable for the high-load test regime.

3. RESULTS AND DISCUSSION

3.1. Structural Characterization. The structure and composition of the interface between the substrate and film are investigated to understand the mechanism of adhesion. Figure 3 shows a bright-field STEM image of the interface between the DLC film and substrate after the Si implantation process. An AES depth profile of each element in the interface layer is also presented. As shown in Figure 3a,b, a 52 nm thin transition layer is observed between the film and substrate as a medium-gray area. A close inspection of the interface layer reveals two regions: Fe−Si−O (region 1) and Si (region 2). The observed Fe−Si−O layer with a thickness of 18 nm corresponds to the ion-implantation layer formed during the initial stage of ion implantation. This result agrees well with the ion range of Si with 18 keV energy into the 304 stainless steel substrates (according to SRIM 200 soft, IBM). The 27 nm Si layer is formed during the late stage of ion implantation. The observed O is attributed to the destruction of the oxide layer on the substrate surface by Si ion implantation. HRTEM

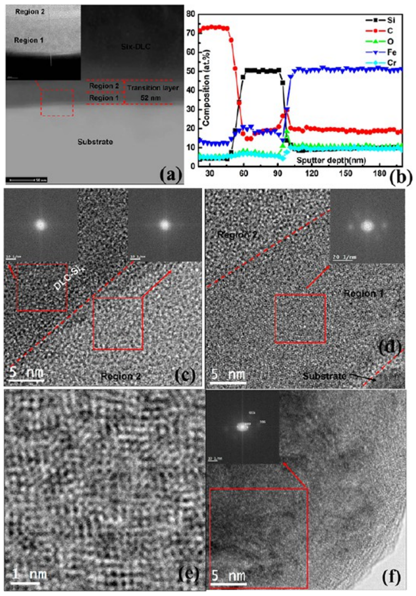

Figure 3. (a) STEM image and (b) AES spectra of the interface between the coating and substrate. (c) HRTEM image of the interface between region 2 and Si_x-DLC. (d) HRTEM image of the interface between regions 2 and 1. (e) Inverse-filtered FFT local image of the selected area (red box) given in part d. (f) HRTEM image of the interface between region 1 and the substrate. The insets in parts c, d, and f show the corresponding FFT images of the selected area (red box).

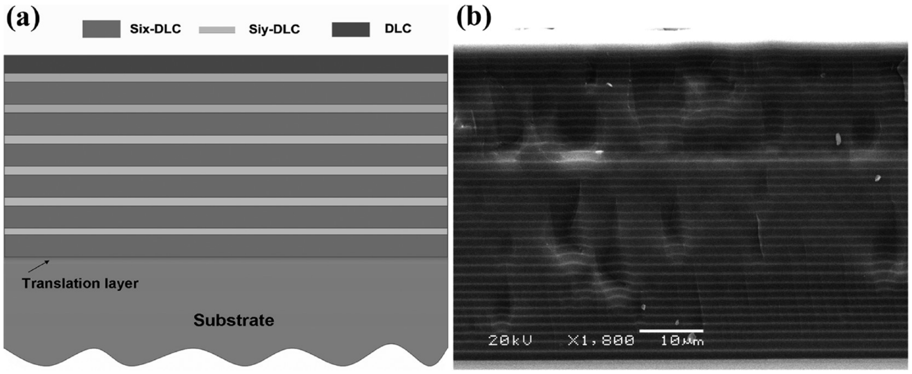

Figure 4. (a) Schematic view of the (Si$_x$-DLC/Si$_y$-DLC)$_n$/DLC film on the substrate and (b) SEM cross section of the (Si$_x$-DLC/Si$_y$-DLC)$_n$/DLC film with a thickness of 52.8 μm.

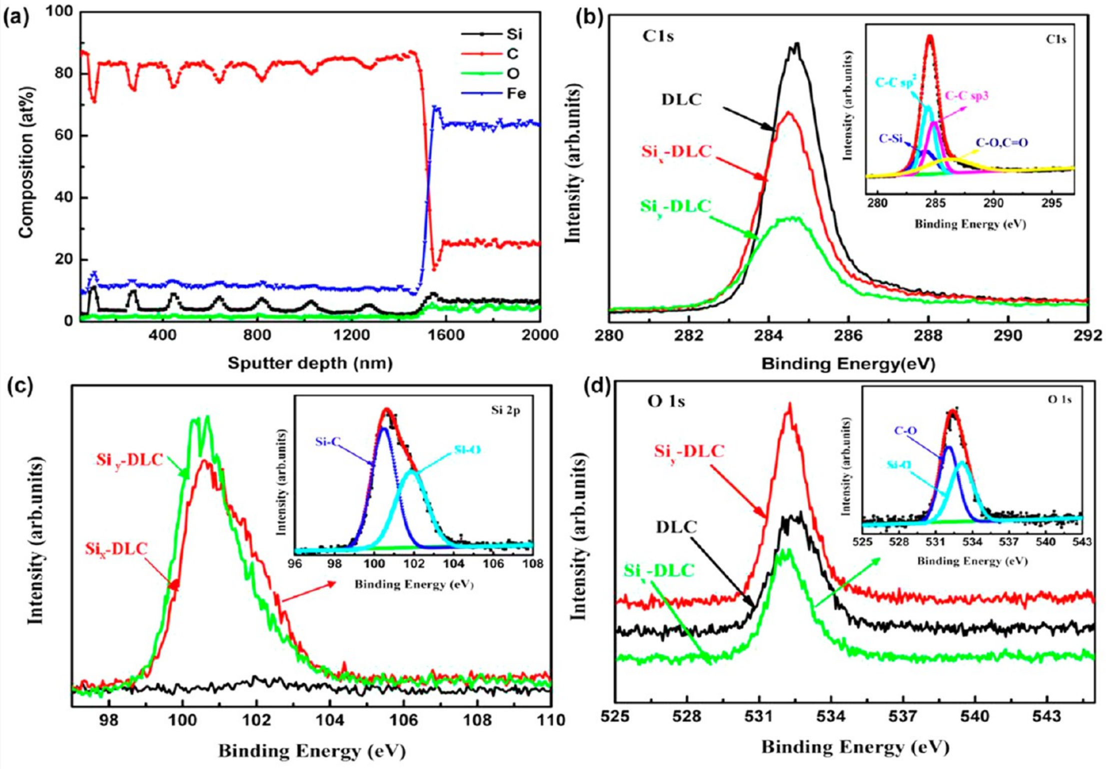

Figure 5. (a) AES spectra of the (Si$_x$-DLC/Si$_y$-DLC)$_n$/DLC film and chemical states of C 1s, Si 2p, and O 1s of Si$_x$-DLC, Si$_y$-DLC, and DLC, respectively: (b) C 1s; (c) Si 2p; (d) O 1s. The insets in parts b−d show the corresponding deconvoluted C 1s, Si 2p, and O 1s XPS spectra of Si$_x$-DLC, respectively.

investigation and selected-area FFT patterns are used to obtain more accurate information, as shown in Figure 3. The diffuse cloudy FFT patterns of the DLC-Si film and region 2 indicate the absence of crystalline phases. Therefore, the deposited DLC-Si film and Si layer are consistent with the amorphous nature, whereas the Fe−Si−O layer shows an unclear crystal structure, i.e., the amorphous-like phase structure, which is a mixed phase of amorphous and crystal (Figure 3d). The formatted Fe−Si−O layer may be due to high-energy ion implantation into the substrate and leads to substrate crystal structure damage. The crystal lattice constant in region 2 is 2.45 Å, which corresponds to the (100) crystal plane of Fe. The formatted translation layer probably reduces the interfacial free energy and decreases the mismatch between the film and substrates, thereby increasing the work of delamination and improving film adhesion.

Figure 4a presents a schematic of the (Si$_x$-DLC/Si$_y$-DLC)$_n$/DLC film on the substrate. Figure 4b shows a SEM image of a (Si$_x$-DLC/Si$_y$-DLC)$_n$/DLC film cross section with a total thickness of about 52.2 μm deposited by PHC-PECVD. The total deposition time for the growth of this structure is 16 h. A cyclical layer consisting of Si$_x$-DLC, Si$_y$-DLC, and a pure DLC top layer constitutes the full (Si$_x$-DLC/Si$_y$-DLC)$_n$/DLC film. No cracks or delaminations can be detected at the interfaces. AES analysis confirms that the Si$_x$-DLC, Si$_y$-DLC, and DLC top layers had thicknesses of about 1.1 ± 0.1, 0.3 ± 0.1, and 1.1 ± 0.1 μm, respectively (Figure 5a). The average deposited rate is determined at 3.1 μm/h. Each element possesses a unique set of bonding energies, and XPS offers a reliable analysis of the chemical state of the constituent elements. Therefore, the chemical compositions of Si$_x$-DLC, Si$_y$-DLC, and DLC are characterized by XPS.

Parts b−d of Figure 5 show the XPS spectra of the Si_x-DLC, Si_y-DLC, and DLC film elements. The survey spectrum shows that the Si_x-DLC and Si_y-DLC films consist of carbon, Si, and oxygen. As expected, the DLC film consists of carbon and oxygen. The compositions of the constituents are as follows: 82.3 atom % C, 7.1 atom % Si, and 7.1 atom % O for Si_x-DLC; 71.4 atom % C, 10.7 atom % Si, and 14.8 atom % O for Si_y-DLC; 92.9 atom % C and 7.1 atom % O for the pure DLC film. For two concentrations of Si on the Si-DLC film, the C 1s spectrum exhibits a nearly symmetric line shape centered around 284.5 eV. C 1s spectra are fitted by decomposing each into several components with Gaussian line shapes. The peaks of the bonding energies 284.2, 283.7, and 286.5 eV correspond to sp^3 C−C bonds, sp^2 C−C bonds, and O−C−O bonds, respectively.[32,33] The peaks of the bonding energies at 282.9 eV may be contributed by the Si−C bond.[32] The peaks for Si 2p can be resolved into two contributions: one at 102.8 eV and another at around 100.3 eV, approximately. The peak with a lower binding energy is consistent with the Si−C bonds.[34] The peak with a higher binding energy mostly rises from the presence of Si bonded to O.[29] The Si 2p spectrum reveals that the Si−C bond predominantly exists with a minor portion of the Si−O bond. The peaks for O 1s spectrum can also be resolved into two components with Gaussian line shapes. The peak centered at about 532 eV is assigned to Si−O bonding,[32] and the lower binding energy is attributed to C−O bonding in the range of 530.5−531.5 eV.[29] For the pure DLC film, the peaks for C 1s at the bonding energies 284.2, 283.7, and 286.5 eV correspond to sp^2 C−C, sp^3 C−C, and C−O bonds, respectively. The O 1s spectrum exhibits an asymmetric line shape centered at 530 eV, which is assigned to C−O bonding.[34] The XPS results indicate that C−C and Si−C bonds dominantly exist on the Si-doped DLC film, whereas Si−O and C−O bonds are contributed in lower amounts. The residual stress of the Si-DLC film may be tailored by the choice of different Si−C bonds in the DLC film.

3.2. Mechanical Properties of the (Si_x-DLC/Si_y-DLC)$_n$/DLC Films.

Figure 6 shows the hardness values of the (Si_x-DLC/Si_y-DLC)$_n$/DLC films as a function of the thickness. Given that the maximum penetration depth is less than 1/10 of the film thickness, which corresponds to about 150 nm, the observed hardness reflects the actual hardness of DLC itself with a slight effect of the substrate material. The (Si_x-DLC/Si_y-DLC)$_n$/DLC film with a thickness of 2.3 μm exhibits a hardness of about 9.1 GPa. However, hardness increases gradually as the thickness increases. The maximum value of 23 GPa is obtained when the thickness reaches 52.2 μm. These changes indicate that the hardness of the film is increased by increasing thickness. This phenomenon may be related to the toughness of the films. Kodli et al.'s research[35] indicated that DLC coatings were found to have a linear relationship between the hardness and fracture toughness unlike the conventional relationship typically observed between the fracture toughness and hardness. Subramanian and Strafford[31] suggested that a multilayer structure could improve the film fracture toughness because cross-sectional cracks could be terminated by their deflection at interfaces and braking in a ductile layer with energy dissipation by plastic deformation. The toughness of thick multilayer films is better than those of thin films. Therefore, compared with the thin DLC films, the thick films have a higher hardness.

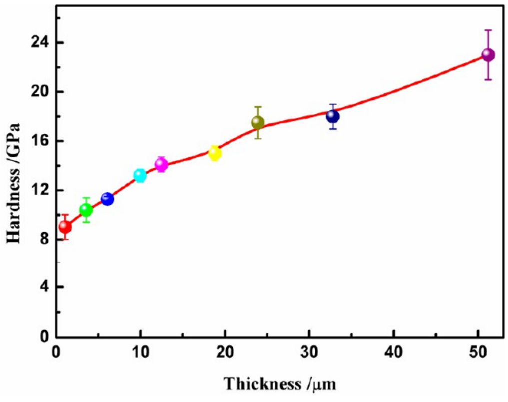

Figure 6. Hardness as a function of the thickness.

The adhesive strength of the DLC film prepared with different thicknesses is evaluated by gradually increasing the load of the diamond stylus. In the evaluation of the adhesion strength by the scratch test, the critical load L_c is defined as the load where the initial crack forms, with sharp increases of the friction force and acoustic emission. Figure 7 shows the critical load as a function of the thickness of the DLC films. As shown in Figure 7, the thick film has a much higher critical load than that of the thin film. The critical load is only 4.6 N when the thickness is about 2.3 μm, and the critical load increases slowly to 9.8 N as the thickness increases to 18.8 μm. When the thickness exceeds 20 μm, the critical load sharply increases. The maximum value of 57 N is obtained when the thickness reaches 52.2 μm. This is probably because thick DLC films have higher hardness and higher load-bearing capacity than thin films (high load-bearing capacity will be discussed in the FEM simulation results). The difficulty of diamond stylus penetration in the film increases with the thickness of the DLC film.

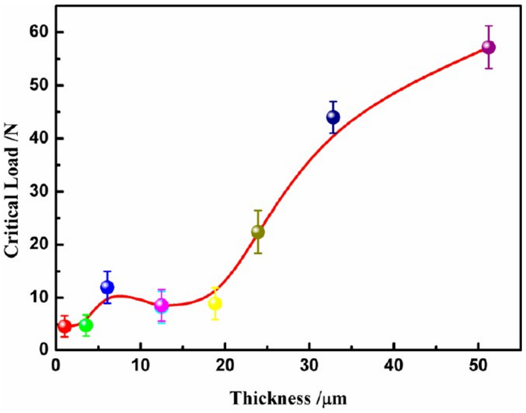

Figure 7. Critical load as a function of the thickness.

In the scratch test, the sample undergoes elastic and plastic deformation, and the film fails in various ways because of the large quantity of strain energy introduced to the film around the diamond stylus. Results show a similar film failure mechanism for all prepared multilayer films in this study. Figure 8 presents typical SEM micrographs of the different failures occurring in a scratch track. At a relatively low load (Figure 8a,b), tensile and conformal cracks are examined in the region of the scratch track. In addition, no chips are determined. First, tensile cracks with a mirror image of the trailing edge of the indenter appear superficially below the indenter. These cracks result from tensile frictional stresses

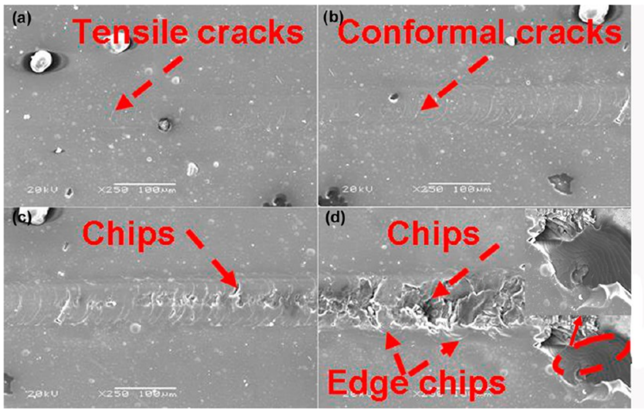

Figure 8. Failure modes in the scratch test in plan views: (a) tensile cracking; (b) conformal cracking; (c and d) chipping failure.

behind the trailing edge of the stylus. These stresses balance the compressive frictional stresses in front of the stylus. Second, conformal cracks follow semicircular trajectories parallel to the leading edge of the indenter. These cracks form in front of the indenter as plastic deformation of the film and underlying substrate, causing a tensile bending moment on the film. Both types of cracks mentioned previously represent remaining failures because they occur while the film is fully adherent. At a relatively high load, the chips are embedded at the bottom of the track beside the tensile and conformal cracks, as shown in Figure 8c. Edge chips occur by further increasing the load because of large bending stress on the scratch sides (Figure 8d). Finally, the films completely peel off from the substrates.

The residual stress of the (Si_x-DLC/Si_y-DLC)$_n$/DLC films is tested by an interferometry. The effect of residual stress and adhesion due to the formation of translation is examined. Without implantation (intermediate layers), the film (about 1 μm) is spontaneously delaminated from the substrate during removal from the deposition chamber. Under this condition, a stable DLC film for testing residual stress cannot be obtained. These occurrences suggest that the DLC film deposited without an intermediate layer shows considerable residual stress and low adhesive strength. This finding may be due to the mismatch of thermal expansion coefficients (thermal expansion of the DLC film of about 1×10^{-6}/K and of steel of about 11.8×10^{-6}–14.71×10^{-6}/K).[21] Residual stresses in films arise from the contribution and interaction of two main sources: thermal stress and intrinsic stress.[36−38] Any mismatch in the thermal expansion coefficient between the film and substrate causes thermal stress. With implantation, the residual stress for the single DLC layer with a thickness of 1 μm is −0.45 GPa (Figure 9). The residual stress of the film is reduced by forming a thin transition layer between the substrate and DLC films, which consists of an amorphous-like Fe−Si−O layer and an amorphous Si layer. Despite this reduction, a single DLC film with a thickness of 6 μm on 304 stainless steel substrates starts to break up and peel off from the substrate.

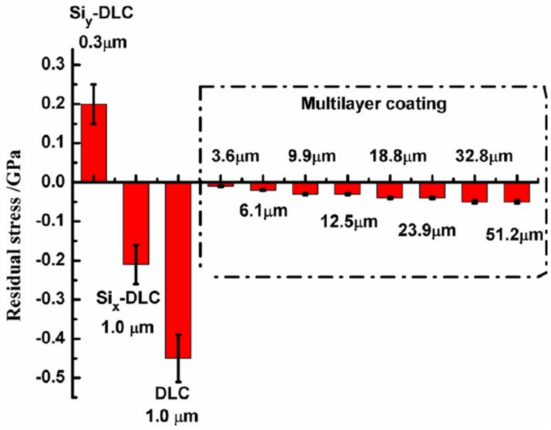

Figure 9. Residual stress of single and (Si_x-DLC/Si_y-DLC) $_n$/DLC films as a function of the thickness.

To prepare a much thicker film, residual stress must be reduced further. The residual stresses for Si_x-DLC and Si_y-DLC films are calculated at about −0.21 and 0.20 GPa, respectively (Figure 9). This finding suggests that the residual stress in the film can be decreased by incorporating a Si element. Moreover, the Si-DLC film with tensile stress and compressive stress can be obtained by choosing distinct contents of the Si−C bonds in the film. The residual stress in the film can be reduced further by formation of the tensile stress/compressive stress structure called the (Si_x-DLC/Si_y-DLC)$_n$/DLC film. Figure 9 shows the residual stresses of the (Si_x-DLC/Si_y-DLC)$_n$/DLC film. The residual stress in this film with a thickness of 2.6 μm is only about −0.01 GPa. Despite the increase in the thickness of the film up to 52.2 μm, the residual stress remains lower than −0.05 GPa. This result indicates that the almost stress-free DLC film is deposited by designing a tensile stress/compressive stress structure. Figure 10 presents a schematic of the mechanism of low residual stress in this structure. The residual stress for Si_y-DLC and DLC films is tensile stress, whereas that for the Si_x-DLC film is compressive stress. Thus, the directions of strains occurring in Si_x-DLC and Si_y-DLC are opposite. However, the adhesion strength between Si_x-DLC and Si_y-DLC is sufficiently tough. The strain does not cause peeling off of the Si_x-DLC film from the Si_y-DLC film. Thus, the residual stress relaxes in this approach, and low residual stress is finally obtained.

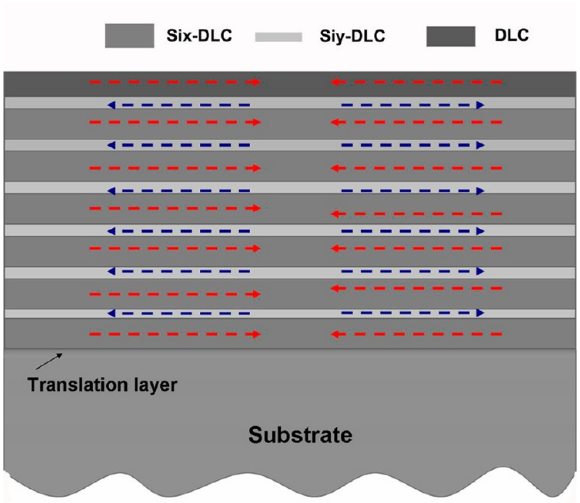

Figure 10. Schematic illustration of the mechanism of low residual stress in a (Si_x-DLC/Si_y-DLC) $_n$/DLC film.

3.3. Tribological Performance and Load-Bearing Capacity of the (Si_x-DLC/Si_y-DLC)$_n$/DLC Films. The tribological properties of the as-deposited (Si_x-DLC/Si_y-DLC)$_n$/DLC films with a thickness of 24.4 μm are determined by a reciprocating wear test under different lubricated conditions, namely, air, water, and oil. The counterpart was a hardened (HRC 60-62) GCr 15 steel ball with a diameter of 6 mm. The sliding speed was 50 mm/s, and the normal load was 10 N. All of the tests were conducted at room temperature of about 24 ± 2 °C and a relative humidity of 20−30%. Figure 11 shows the results of variation of the friction coefficient with the tested time. An initial friction coefficient of 0.21 is observed under air conditions, which increases to a final steady-state friction of 0.24. The friction coefficients under water and oil-lubricated conditions are lower than those under dry conditions. After the running process, the average friction coefficients for water- and oil-lubricated environments are calculated at 0.02 and 0.03, respectively. These results can be explained by the lubricating effect of discontinuous water or an oil film between the partial solid−solid contact faces.[39,40] Figure 12 shows the micrographs of wear tracks on the films after reciprocating wear tests. The morphologies of wear tracks under different lubricated conditions are distinct. The wear track under dry conditions seems to show small pieces of film being peeled off of the substrate on random delaminated microregions, whereas the nondelaminated microregions are very smooth. The depth of the wear track measures about 0.4 μm. Several unexpected partial delaminations and cracking are observed within the wear track when sliding water lubricates the environment; however; the wear scar depth seems shallower than the wear track under dry conditions. For the wear track under oil-lubricated conditions, almost no delamination or film crack is observed besides the wear tracks. The wear track mainly consists of slight grooves and a shallow depth (about 200 nm). Although the wear track under dry and water-lubricated conditions reveals delaminations and cracks, the wear rate remains low. The wear rates under dry, wet, and oil-lubricated conditions are approximately 8.4×10^{-14}, 1.0×10^{-15}, and 7.5×10^{-15} m^3/N·m, respectively. These results suggest that (Si$_x$-DLC/Si$_y$-DLC)$_n$/DLC films are potential protective surfaces under the dry, water, and oil-lubricated conditions.

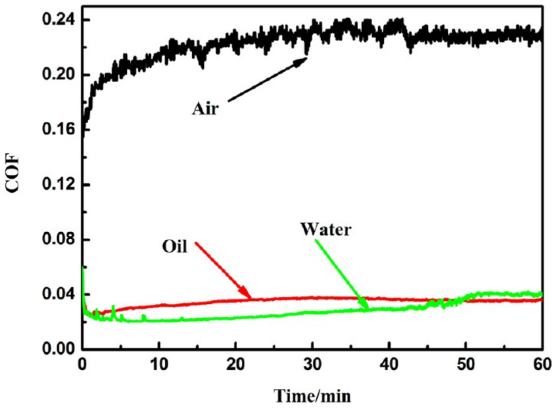

Figure 11. Friction coefficient as a function of the tested time under air, oil, and water environments.

The curve of the friction coefficient changes as a function of the applied loads, as shown in Figure 13. The friction coefficient of the (Si$_x$-DLC/Si$_y$-DLC)$_n$/DLC film starts at a low value at the beginning of sliding and quickly increases to a steady state (in the range of 0.15−0.21). Clearly, the (Si$_x$-DLC/Si$_y$-DLC)$_n$/DLC film exhibits a direct relation between the normal load and steady friction coefficient: the larger the applied load, the lower the coefficient of friction. This phenomenon can be interpreted by an adhesion mechanism associated with a change in the contact area:[41]

$$\mu = S\frac{A}{L} \tag{1}$$

where S is the shear strength between the surfaces in contact, A is the contact area, and L is the normal load. In elastic (Hertzian) conditions, the contact area depends on the load as $A \propto L^n$, with $n = {}^2/_3$ for a circular contact (sphere on plane). Thus, eq 1 can be rewritten as follows:

$$\mu = KL^x \qquad -1 < x < 0 \tag{2}$$

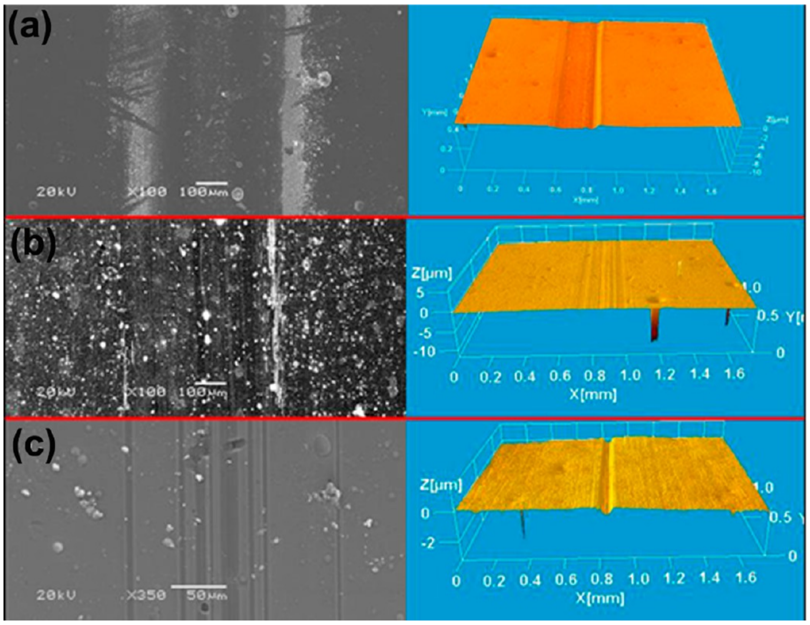

Figure 12. SEM and optical 3D surface morphologies on a worn track with different conditions: (a) air; (b) water-lubricated; (c) oil-lubricated.

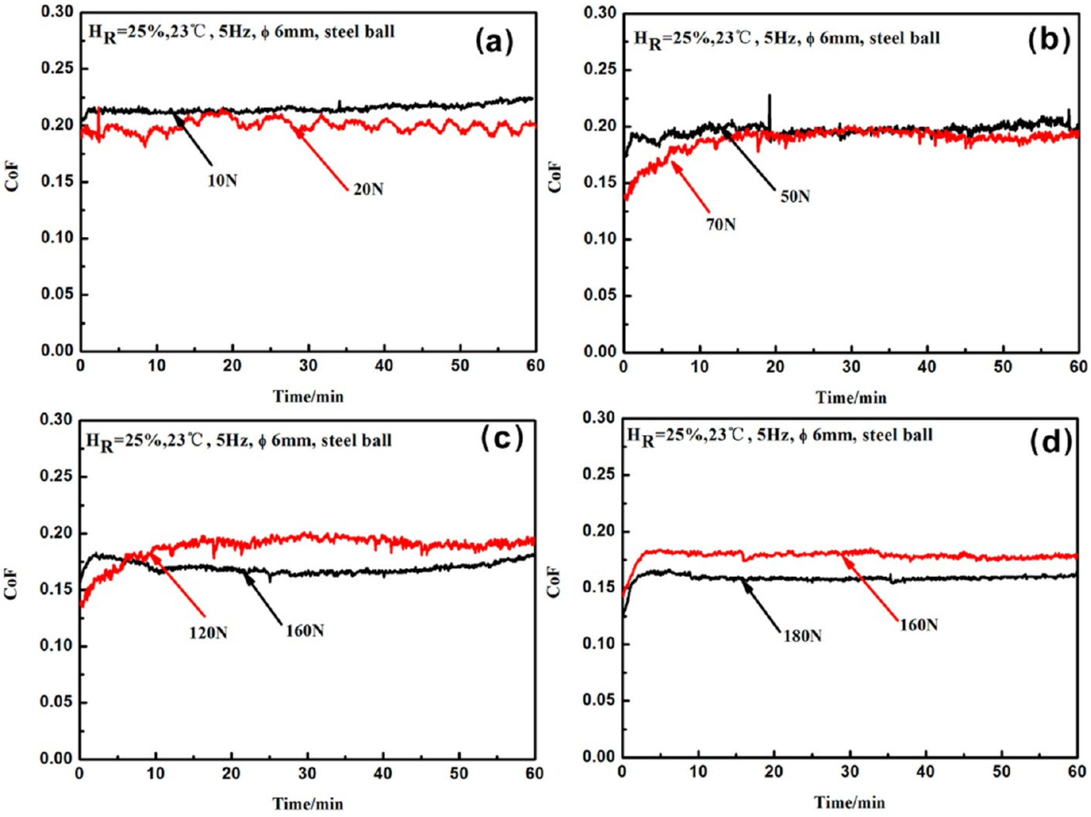

Figure 13. Friction coefficient as a function of the applied load with different thicknesses: (a) 2.6 μm; (b) 9.4 μm; (c) 34.8 μm; (d) 52.2 μm.

Figure 13 also presents the maximum applied load that the films can be subjected to during tribological tests. For (Si$_x$-DLC/Si$_y$-DLC)$_n$/DLC with a thickness of 2.6 μm, the film is not destroyed after the tests at the load of 20 N. Failure only occurs when the load is increased to 30 N. Thus, the maximum applied load of (Si$_x$-DLC/Si$_y$-DLC)$_n$/DLC with a thickness of 2.6 μm is only about 20 N (1.5 GPa). However, the maximum applied load increased to 70 N (2.3 GPa), 160 N (3.0 GPa), and 180 N (3.2 GPa) for the (Si$_x$-DLC/Si$_y$-DLC)$_6$/DLC film (thickness: 9.6 μm), (Si$_x$-DLC/Si$_y$-DLC)$_{24}$/DLC film (thickness: 34.8 μm), and (Si$_x$-DLC/Si$_y$-DLC)$_{44}$/DLC film (thickness: 62.8 μm), respectively. This finding suggests that thick (Si$_x$-DLC/Si$_y$-DLC)$_n$/DLC films exhibit high load-bearing capability. Table 2 lists values for the load-bearing capability of coated surfaces. Generally, the DLC film fails under a contact pressure of 1 GPa, and a higher value can be obtained at 2.6 GPa. In this study, thick (Si$_x$-DLC/Si$_y$-DLC)$_n$/DLC films can run at pressures of 3.2 GPa, probably because of the increased thickness and the multilayered structure of the film. To confirm this observation, a FEM was used to simulate the stress distribution in the multilayer DLC film under the test condition using ANSYS Multiphysics (*ANSYS v8.2*, ANSYS, Inc.).[48,49]

Table 2. Some Values for the Load-Bearing Capability of Coated Surfaces in Literatures

film/substrate	counterpart	max load (N)	contact pressure (GPa)	reference
Graphit-iC coatings/ M42 tool steel	WC-6% Co ball, Φ5 mm	80	2.1	42
Cr-DLC/Cr/high-speed steel	alumina ball, Φ9 mm	95	2.0	43
Cr-DLC/BDO/Ti$_6$Al4V	alumina ball, Φ8 mm	180	2.6	44
DLC/Cr/M42 tool steel	WC-6% Co ball, Φ5 mm	80	2.1	45
multilayered DLC-CrN/ TPN-treated Ti6Al4V	100Cr6 steel ball, Φ 10 mm	5	∼1.0	46
multilayered (DLC/ Cr)$_n$/M2 high-speed steel	Al$_2$O$_3$ ball, Φ 6 mm	50	∼1.0	47

Figure 14 presents the FEM simulation results. First, when a load is applied (30 N) on the steel ball (Figures 2), a high compressive stress concentration occurs at the substrate–film

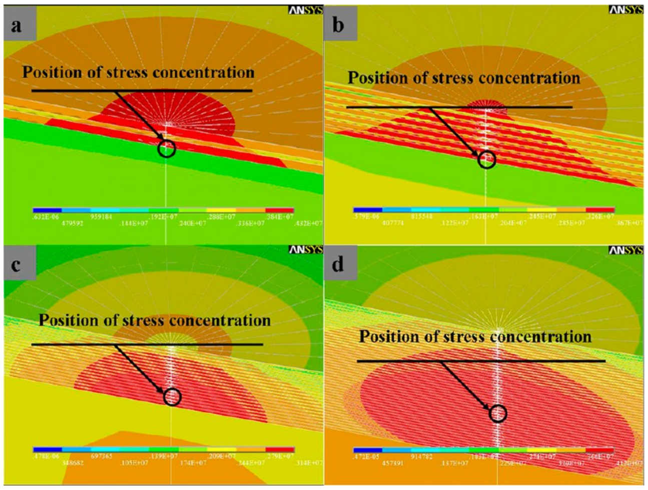

Figure 14. Contour plots of the von Mises stress for a (Si$_x$-DLC/Si$_y$-DLC)$_n$/DLC-coated system with different thicknesses: (a) 2.6 μm; (b) 9.6 μm; (c) 34.8 μm; (d) 62.8 μm.

interface (parts a and b). As the thickness increases, the position of the maximum stress where the mostly likely occurrence of fracture is moves into the film away from the substrate−film interface (parts c and d), and the maximum stress of the surface is simultaneously decreased. It is well-known that the whole film fails mainly because of substrate−film interface failure. Therefore, these thin films are more likely to fail compared with the thick DLC film. Second, a distinct difference stress field is observed in the Si_x-DLC and Si_y-DLC films because of differences in elastic moduli. The stress value of the Si_x-DLC layer is more than that of the Si_y-DLC layer. The difference in the stress field between two alternating layers may influence the direction of crack propagation. The generated microcracks branch and deflect at the interface. Obviously, the thicker film has more interfaces, which will consume more energy in the process of crack propagation from surface to substrate. On the basis of the above two points, the superthick DLC films will present an ultrahigh load-bearing capacity.

These superthick films exhibit high hardness, ultrahigh load-bearing capability, and low friction. These properties protect the coated substrate, indicating that these hard solid lubricant films meet the requirements of a wide range of applications. These kinds of superthick films (about 20 μm) with ultrahigh load-bearing capability have been successfully deposited on internal surfaces of pipes, piston rings, pistons, and cylinder heads (Figure 15). The coated surfaces are uniform, smooth, and compact. The servicing life and failure processes of parts of coated surfaces are under investigation regarding related mechanical parts. Further investigations on the corrosion resistance and thermal stability, among others, need to be conducted.

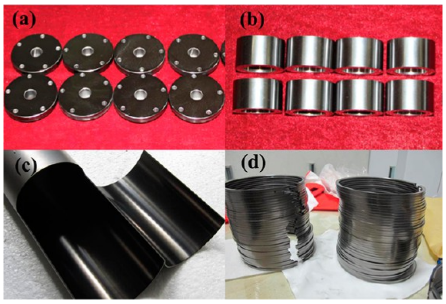

Figure 15. $(Si_x\text{-DLC}/Si_y\text{-DLC})_n$/DLC-coated surfaces with film thickness of approximately 20 μm: (a) cylinder heads; (b) pistons; (c) internal surfaces of pipes; (d) piston rings.

4. CONCLUSION

The PHC-PECVD method allows deposition of superthick $(Si_x\text{-DLC}/Si_y\text{-DLC})_n$/DLC films with thickness of more than 50 μm. Prior to deposition, a translation layer between the substrate and film can significantly reduce the internal stress. The tensile stress/compressive stress structure reduces the future residual stress. The thick $(Si_x\text{-DLC}/Si_y\text{-DLC})_n$/DLC film exhibits superior mechanical properties. The hardness and adhesion strength of the film are measured up to 22 GPa and 65 N, respectively. In addition, the thick DLC film exhibits high sliding wear resistance and low friction in three environments, namely, air, water, and oil. Given that the position of maximum stress moves toward the film and away from the substrate−film interface with an increase in the thickness, generated cracks are away from the interface and located on the surface of the film. Therefore, an ultrahigh load-bearing capacity as high as 3.2 GPa can be obtained. These parameters are rather unusual relative to the current understanding of processing routes for DLC films and expand the scope and range of potential for commercial applications that can exploit the combined properties of high hardness, low friction, low wear, and high load-bearing capacity.

AUTHOR INFORMATION

Corresponding Author

*Tel/Fax: +86 9364968080. E-mail: lpwang@licp.cas.cn.

Notes

The authors declare no competing financial interest.

ACKNOWLEDGMENTS

The authors are grateful for financial support from the National Natural Science Foundation of China (Grant 11172300). The authors gratefully acknowledge Yaonan Zhang and Guohui Zhao for supporting the numerical simulation at the Lanzhou branch of supercomputing CAS.

REFERENCES

(1) Robertson, J. *Prog. Solid State Chem.* **1991**, *21*, 199−333.
(2) Thomson, L. A.; Law, F. C.; Rushton, N.; Franks, J. *Biomaterials* **1991**, *12*, 37−40.
(3) Dwivedi, N.; Kumar, S.; Tripathi, R. K.; Carey, J. D.; Malik, H. K.; Dalai, M. K. *ACS Appl. Mater. Interfaces* **2012**, *4*, 5309−5316.
(4) Robertson, J. *Mater. Sci. Eng., R* **2002**, *37*, 129−281.
(5) Ma, S. L.; Ma, D. Y.; Guo, Y.; Xu, B.; Wu, G. Z.; Xu, K. W.; Chu, P. K. *Acta Mater.* **2007**, *55*, 6350−6355.
(6) Müller, U.; Falub, C. V.; Thorwarth, G.; Voisard, C.; Hauert, R. *Acta Mater.* **2011**, *59*, 1150−1161.
(7) Endrino, J. L.; Marco, J. F.; Allen, M.; Poolcharuansin, P.; Phani, A. R. *Appl. Surf. Sci.* **2008**, *254*, 5323−5328.
(8) Vila, M.; Carrapichano, J. M.; Gomes, J. R.; Camargo, S. S.; Achete, C. A.; Silva, R. F. *Wear* **2008**, *265*, 940−944.
(9) Bobzin, K.; Bagcivan, N.; Goebbels, N.; Yilmaz, K.; Michaelis, K.; Hochmann, M. *Surf. Coat. Technol.* **2009**, *204*, 1097−1101.
(10) Bouzakis, K. D.; Hadjiyiannis, S.; Skordaris, G.; Anastopoulos, J.; Mirisidis, I.; Michailidis, N.; Efstathiou, K.; Knotek, O.; Erkens, G.; Cremer, R.; Rambadt, S.; Wirth, I. *Surf. Coat. Technol.* **2003**, *174−175*, 393−401.
(11) Bouzakis, K. D.; Hadjiyiannis, S.; Skordaris, G.; Mirisidis, I.; Michailidis, N.; Erkens, G. *Surf. Coat. Technol.* **2004**, *188−189*, 636−643.
(12) Siu, J. H. W.; Li, L. K. Y. *Wear* **2000**, *23*, 283−287.
(13) Holmberg, K.; Laukkanen, A.; Ronkainen, H.; Wallin, K.; Varjus, S.; Koskinen, J. *Surf. Coat. Technol.* **2006**, *200*, 3810−3823.
(14) Villiger, P.; Sprecher, C.; Peters, J. A. *Surf. Coat. Technol.* **1999**, *116/119*, 585−590.
(15) Grill, A. *Diamond Relat. Mater.* **1999**, *8*, 428−434.
(16) Chang, C. L.; Wang, D. Y. *Diamond Relat. Mater.* **2001**, *10*, 1528−1534.
(17) Chen, K. W.; Lin, J. F. *Thin Solid Films* **2009**, *517*, 4916−4920.
(18) Kim, H. J.; Moon, M. W.; Kim, D. I.; Lee, K. R.; Oh, K. H. *Scr. Mater.* **2007**, *57*, 1016−1019.
(19) Panat, R.; Zhang, S.; Hsia, K. J. *Acta Mater.* **2003**, *51*, 239−249.
(20) Ulrich, S.; Theel, T.; Roth, H.; Ehrhardt, H.; Becker, P.; Silva, S. R. P. *J. Appl. Phys.* **1997**, *82*, 6024−6030.
(21) Silva, W. M.; Trava-Airoldi, V. J.; Chung, Y. W. *Surf. Coat. Technol.* **2011**, *205*, 3703−3707.
(22) Tarrant, R. N.; Montross, C. S.; McKenzie, D. R. *Surf. Coat. Technol.* **2001**, *136*, 188−191.
(23) Schwarz, C.; Heeg, J.; Rosenberg, M.; Wienecke, M. *Diamond Relat. Mater.* **2008**, *17*, 1685−1688.

(24) Wilhelmsson, O.; Rasander, M.; Carlsson, M.; Lewin, E.; Sanyal, B.; Wiklund, U.; Eriksson, O.; Jansson, U. *Adv. Funct. Mater.* **2007**, *17*, 1611−1616.
(25) Wang, Y. F.; Wang, J.; Zhang, G. A.; Wang, L. P.; Yan, P. X. *Surf. Coat. Technol.* **2012**, *206*, 3299−3308.
(26) Zou, Y. S.; Wang, Q. M.; Du, H.; Song, G. H.; Xiao, J. Q.; Gong, J.; Suna, C.; Wen, L. S. *Appl. Surf. Sci.* **2005**, *241*, 295−302.
(27) Vila, M.; Carrapichano, J. M.; Gomes, J. R.; Camargo, S. S., Jr.; Achete, C. A.; Silva, R. F. *Wear* **2008**, *265*, 940−944.
(28) Ban, M.; Hasegawa, T.; Fujii, S.; Fujioka, J. *Diamond Relat. Mater.* **2003**, *12*, 47−56.
(29) Takeshita, T.; Kurata, Y.; Hasegawa, S. *J. Appl. Phys.* **1992**, *71*, 5395.
(30) Holleck, H.; Schier, V. *Surf. Coat. Technol.* **1995**, *76−77*, 328−336.
(31) Subramanian, C.; Strafford, K. N. *Wear* **1993**, *165*, 85−95.
(32) Lee, W. Y. *J. Appl. Phys.* **1980**, *51*, 3365−3372.
(33) Zhou, S. G.; Wang, L. P.; Lu, Z. B.; Ding, Q.; Wang, S. C.; Wood, R. J. K.; Xue, Q. J. *J. Mater. Chem.* **2012**, *22*, 15782−15792.
(34) Moulder, J. F.; Stickle, W. F.; Sobol, P. E.; Bomben, K. D. *Handbook of X-ray Photoelectron Spectroscopy*; Perkin-Elmer Corp.: Waltham, MA, 1992.
(35) Kodli, P.; Walter, K. C.; Nastasi, M. *Tribol. Int.* **1997**, *30*, 591−598.
(36) Pauleau, Y. *Vacuum* **2001**, *61*, 175−181.
(37) Knuyt, G.; Lauwerens, W.; Stals, L. M. *Thin Solid Films* **2000**, *370*, 232−237.
(38) Teixeira, V. *Thin Solid Films* **2001**, *392*, 276−281.
(39) Nogueira, I.; Dias, A. M.; Gras, R.; Progri, R. *Wear* **2002**, *253*, 541−549.
(40) Wang, Y. X.; Wang, L. P.; Xue, Q. J. *Surf. Coat. Technol.* **2011**, *205*, 2770−2777.
(41) Bowden, F. P.; Tabor, D. *The friction and lubrication of solids*; Clarendon: Oxford, U.K., 1986.
(42) Stallard, J.; Mercs, D.; Jarratt, M.; Teer, D. G.; Shipway, P. H. *Surf. Coat. Technol.* **2004**, *177*, 545−551.
(43) Zeng, X. T.; Zhang, S.; Ding, X. Z.; Teer, D. G. *Thin Solid Films* **2002**, *420−421*, 366−370.
(44) Zhang, Z. X.; Dong, H.; Bell, T. *Surf. Coat. Technol.* **2006**, *200*, 5237−5244.
(45) Yang, S.; Li, X.; Renevier, N. M.; Teer, D. G. *Surf. Coat. Technol.* **2001**, *142*, 85−93.
(46) Avelar-Batista, J. C.; Spain, E.; Fuentes, G. G.; Sola, A.; Rodriguez, R.; Housden, J. *Surf. Coat. Technol.* **2006**, *201*, 4335−4340.
(47) Yu, X.; Liu, Y.; Wang, C. B.; Lu, X. C.; Yu, D. Y. *Vacuum* **2005**, *80*, 324−331.
(48) Holmberg, K.; Laukkanen, A.; Ronkainen, H.; Wallin, K. *Tribol. Int.* **2009**, *267*, 2142−2156.
(49) Abdul-Baqi, A.; Van der Giessen, E. *Int. J. Solids Struct.* **2002**, *39*, 1427−1442.